Journal of Materials Chemistry C

ROYAL SOCIETY OF CHEMISTRY

PAPER

View Article Online
View Journal | View Issue

Cite this: *J. Mater. Chem. C*, 2025, **13**, 21170

Engineering morphological features and surface steps in ultrathick penta-twinned copper nanowires

Andrea Conte, Sabrina Antonello, Marco Baron, Sara Bonacchi * and Alessandro Aliprandi *

Received 7th May 2025,
Accepted 21st August 2025

DOI: 10.1039/d5tc01835h

rsc.li/materials-c

Controlling and foreseeing copper nanostructure properties remains an open challenge in the field of nanoscience. Here, we elucidate the role of glycine as a templating agent to synthesize ultrathick copper nanowires (CuNWs) with a precise control over their morphology and crystal structure. Comprehensive characterization was carried out using orthogonal technique analyses, such as SEM, HR-TEM, AFM, XRD, and electrochemistry, which enable us to gain a complete insight into both the bulk and the surface properties of the CuNWs. In particular, the synthesized CuNWs exhibited a wide range of diameters, from 65 nm to more than 400 nm, and well-defined exposed surfaces composed of the (100) and (110) crystal facets. This precise control over the physicochemical properties of CuNWs could potentially impact different fields of nanotechnologies, ranging from renewable energy to high-speed electronics.

Introduction

Copper nanowires (CuNWs), with their high surface area to volume ratio and large aspect ratio, exhibit excellent electrical,[1–3] electrocatalytic,[4–7] and mechanical properties.[8,9] These properties make CuNWs highly promising building blocks for assembling next-generation functional materials for advanced electronic and electrochemical devices.[10,11] Recent studies have exploited the intrinsic advantages of CuNWs to optimize self-standing three-dimensional (3D) porous electrodes in flow-through configurations,[9,12] thereby combining copper's intrinsic catalytic properties for critical energy conversion processes,[4,13,14] within a support-free electrode fabrication. Furthermore, CuNWs have also recently gained attention in cuproptosis-based cancer therapy,[15,16] as a smart provider of intracellular copper ions, able to disrupt mitochondrial metabolism and lead to selective cancer cell death.[16] Given the significant technological implications of this nanomaterial, achieving precise control—through synthetic protocols—over the atomic-scale structure of these nanowires is crucial for engineering their surface facets and aspect ratios. Crystal surface defectiveness seems indeed to play a key role in enhancing Cu's catalytic efficiency and selectivity by providing active sites, altering the electronic structure and the nano-environment, and enabling them to promote highly specific electroactivated reaction pathways. Examples can be found in the electrochemical conversion of CO_2 into valuable feedstocks,[5,7,17,18] in CO oxidation,[19] in the O_2 evolution reaction[20] and in the NO_3^- reduction reaction.[21] In bio-application as well, defective Cu surfaces such as grain boundaries, dislocations, and surface steps appear to facilitate the oxidation and dissolution of Cu into ions that ultimately act as anticancer agents.[16] Among the various proposed CuNW

Department of Chemical Sciences, University of Padova, Via F. Marzolo 1, 35131, Padova, Italy. E-mail: sara.bonacchi@unipd.it, alessandro.aliprandi@unipd.it

Alessandro Aliprandi

Alessandro Aliprandi obtained his PhD in 2015 from the Institute of Supramolecular Science and Engineering (ISIS), University of Strasbourg, under the supervision of Prof. Luisa De Cola, where he investigated the self-assembly of luminescent Pt(II) complexes. He then joined the group of Prof. Paolo Samorì for his postdoctoral research, broadening his expertise to low-dimensional materials such as graphene and copper nanowires. He is currently an Associate Professor at the Department of Chemical Sciences (DISC), University of Padua (Italy). His research interests span from electroluminescence and chemiluminescence to photocatalysis and CO_2 valorisation.

synthesis approaches, contemplating physical and electrochemical methods, hydrothermal synthesis, which relies on the controlled reduction of Cu(II) complexes in surfactant-containing aqueous media, offers several advantages in terms of reduced cost, scalability, and environmental sustainability. In a recent work, we demonstrated how, through a design of experiments (DOE) approach, to disclose the relationship between key synthetic parameters and the structural characteristics of the nanowires.[7] Post-synthesis techniques such as electrochemical pulses[9] and chemical etching can be successively exploited to modify CuNWs by introducing steps and defectiveness on the surface; nevertheless, achieving precisely engineered nanostructures through synthesis alone remains an open challenge.[22,23]

Herein, we demonstrate the significant role of glycine, employed as a synthetic additive, in modulating the growth, controlling the diameter distribution, and systematically tuning the ratio of surface facets and steps on the CuNWs. Our findings show that by controlling straightforward, scalable, and solution-based synthetic protocols, we can tailor the crystalline quality, surface morphology, and structural defectiveness of thick penta-twinned CuNWs. A combination of techniques, including SEM, XRD, HR-TEM, and AFM, along with cyclic voltammetry measurements, allowed us to completely characterize the crystal structure of our CuNWs and to gain valuable information about their surface crystal motifs.

Results and discussion

CuNWs were prepared by employing aqueous hydrothermal synthesis using $CuCl_2{\cdot}2H_2O$ as a copper source, a mild and green reductive agent like glucose, and 1-octadecylamine (ODA) and glycine as templating agents. In particular, Zhang *et al.* have demonstrated that ODA plays a crucial role in promoting the anisotropic growth of Cu seed crystals by selectively binding to the (100) facet while leaving the (111) facet exposed.[24]

This arrangement leads to the formation of a five-fold twinned structure with five (100) side surfaces aligned along the ⟨110⟩ direction. Kevin *et al.* have shown that glycine can be used as an additive in the synthesis to modulate the diameter of CuNWs between 55 and 150 nm.[25] To shed light on the growth mechanisms, we put forward the reported literature procedure[25] by varying the type of capping agent as well as the amounts of glucose and glycine. In particular, we used 2 equivalents of glucose and x = 0, 2, 3, 6, and 9 equivalents of glycine with respect to $CuCl_2$ (we denoted CuNWs@X to identify a particular type of CuNW in the series) to carry out the synthesis at 125 °C for 18 h. This method allowed the preparation of a family of NWs tuned in diameter and aspect ratio. Representative scanning electron microscopy (SEM) images of the so-prepared CuNWs are shown in Fig. 1 and Fig. S1. These images show that increasing the quantity of glycine, while keeping the other reagents fixed, led to an increase in the average diameter of the NWs and a wider polydispersity of the diameter distribution (see Fig. S2 for a histogram of diameter distribution). Within our synthetic procedure, the diameter of the CuNWs was tuned up to (400 ± 110) nm, reaching 85% in yield, being competitive with the oxalate-based approach recently reported by Kim *et al.*, where nanowires of 500 nm have been reported.[26] Interestingly, we inferred a linear correlation (eqn (1)) between glycine equivalents and the NW diameter (R^2 = 0.95, Root-(MSE) = 0.81, and p-value of model = 0.005), which provides practical guidance for the production of tailored NWs. The residual plot is reported in Fig. S3.

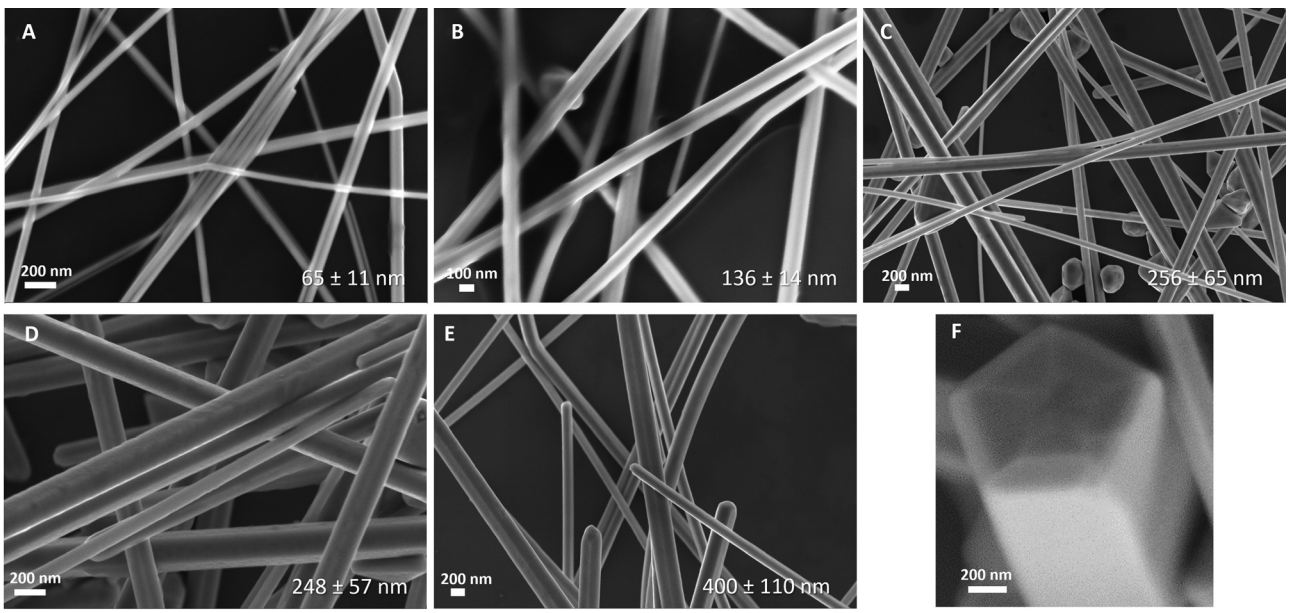

Fig. 1 SEM images of CuNWs synthesized employing different quantities of glycine: (A) 0 eq., (B) 2 eq., (C) 3 eq., (D) 6 eq. and (E) 9 eq. of glycine. (F) Detail of the CuNWs@9 tail highlighting the penta-twinned nature of the CuNWs. The average diameter of CuNWs is highlighted at the bottom of each image.

$$\varnothing\ (\text{nm}) = (65.4 \pm 8.3) + (35.6 \pm 4.9)\cdot\{\text{glycine}\} \quad (1)$$

where $\varnothing$ represents the average diameter of CuNWs, and {glycine} the equivalents of glycine with respect to Cu salt employed during the synthesis.[26] Our protocol allowed us to obtain CuNWs with a yield between 65% and 85% (see Table S1). The SEM images collected allowed us to clearly identify the five twinned prismatic monocrystalline structure of the wires, as shown in Fig. 1F. The boundaries between the five crystal seeds that form the penta-twinned CuNW are well defined, demonstrating the excellent templating properties of the reagents used.

To qualitatively assess the evolution of the hydrothermal synthesis and the effect of the presence of glycine on CuNWs, we monitored the reaction by observing the color changes over time for the synthesis of CuNWs@0 and CuNWs@9, as

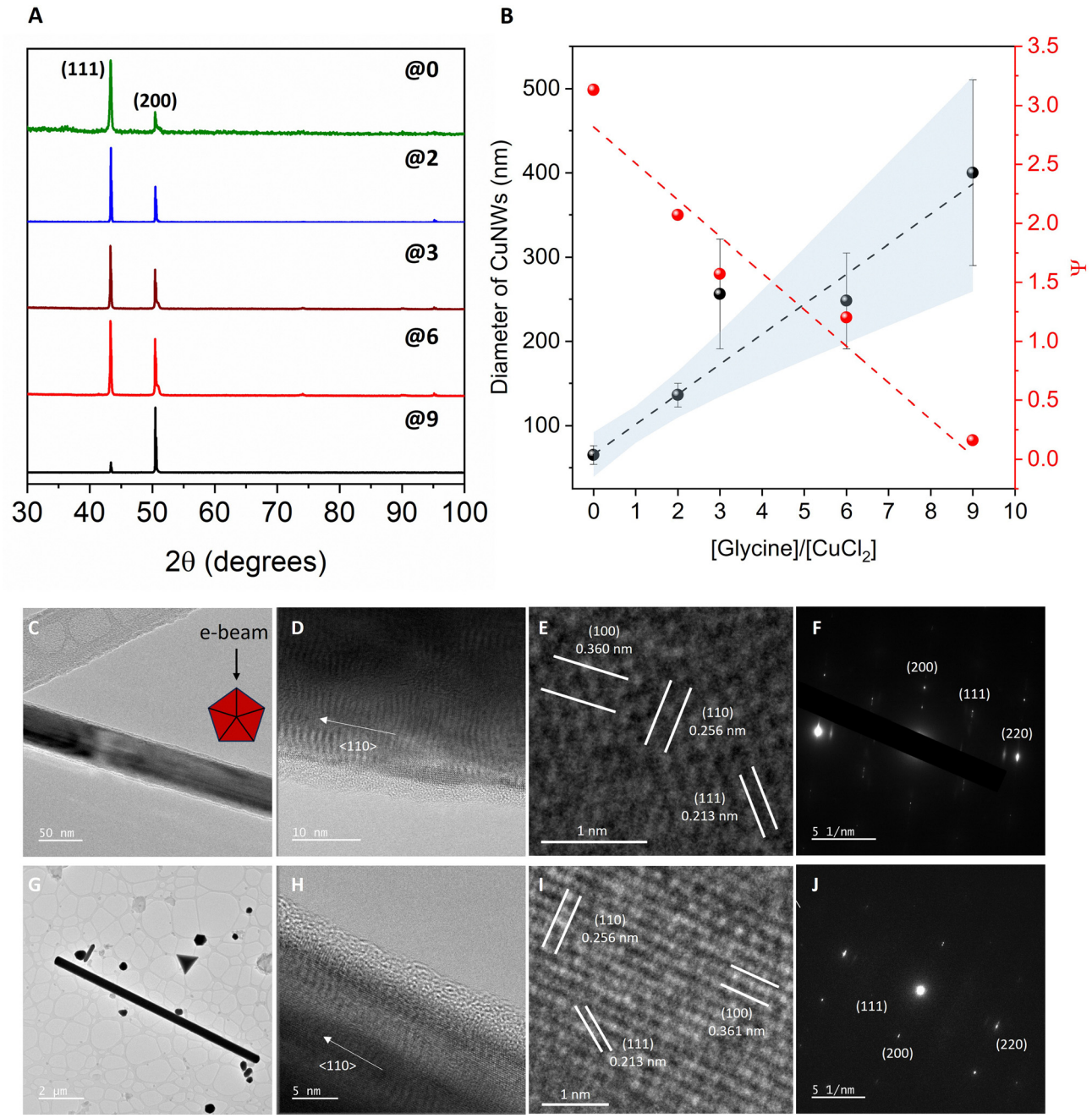

Fig. 2 (A) XRD patterns of CuNWs synthesized with different quantities of glycine: 0 eq. (green), 2 eq. (blue), 3 eq. (dark red), 6 eq. (red), and 9 eq. (black). (B) Plot of the dependence of average diameter of CuNWs (black dots) and of Ψ (red dots) on the equivalents of glycine used in the synthesis. Error bars for diameters are in black and 95% confidence bands are in light blue. (C) TEM image of CuNWs@0. (D) HR-TEM image of CuNWs@0. (E) HR-TEM details of the crystal lattice of CuNWs@0. (F) SAED of single CuNWs@0. (G) TEM image of CuNWs@9. (H) HR-TEM image of CuNWs@9. (I) HR-TEM details of the crystal lattice of CuNWs@9. (J) SAED of single CuNWs@9.

illustrated in Fig. S4. Notably, at the beginning of the reaction, significant differences were observed in terms of color between CuNWs@0 and CuNWs@9. Specifically, the reaction mixture for CuNWs@0 initially appeared light blue after 10 minutes, rapidly transitioned to white, and shortly thereafter turned light brown. Conversely, in the presence of 9 equivalents of glycine, the reaction mixture exhibited an intense electric blue color (due to ligand to metal charge transfer),[27] which progressively deepened before gradually transitioning to dark green, indicating the initial formation of Cu seeds. Ultimately, both reaction mixtures became visually similar, adopting a brownish-red coloration. This observation suggests that the reduction of Cu^{2+} in the presence of glycine may occur primarily through the $Cu(Gly)_2$ complex (characterized by its distinct electric blue color);[28–30] indeed, when glycinate is in excess over Cu in solution, Cu^{2+} glycinate can be reduced to Cu^{+} glycinate with a standard reduction potential of −0.167 V (*vs.* SHE).[28] This cuprous species might be oxidized back to Cu^{2+} glycinate by oxygen in solution and is then available for further oxidation of the CuNWs growing on the surface. This process has the potential to enhance copper dissolution and is well-known as autocatalytic corrosion.[28,31] In contrast, without glycine, the Cu^{2+} cations form a complex with octadecylamine (ODA), specifically $Cu(ODA)_x$.[24,32] Additionally, it was observed that seed formation, indicated by the appearance of the light brown color, occurred more rapidly in the absence of glycine. This may indicate that glycine likely stabilizes the Cu^{2+} cations, thus shifting their reduction potential towards more negative values, therefore making it more difficult to reduce Cu^{2+}.

To compare the crystal structure of the bulk Cu with the morphology of our wires, X-ray diffraction (XRD) was employed (Fig. 2A). For all the CuNW samples, two main peaks were observed at $2\Theta = 43.5^\circ$ and 50.6° corresponding to the (111) and (200) crystal planes of face-centered cubic Cu. The two signals have been exploited to qualitatively investigate the aspect ratio of CuNWs as recently reported by our group.[7] The parameter Ψ, defined as I(111)/I(200) ratio intensity (integral of chosen peaks), is observed to decrease upon increasing the CuNW diameter, as shown in Fig. 2B. Interestingly, thick CuNWs synthesized using 9 equivalents of glycine exhibited a very pronounced (200) facet, while for very thin and long CuNWs, we observed mainly the (111) facet. The observed changes in the XRD intensity ratios are attributed to texture effects, including preferred orientation. These effects become especially evident when comparing CuNWs with very different characteristics. We calculated the aspect ratio for the thicker NWs. The thicker NWs, CuNWs@9, exhibit an average length of (56.5 ± 11.7) μm and an average aspect ratio of 141, which is competitive considering the large diameter (see Table S2). The average length of the other samples was not reported due to technical limitations: bends in the CuNWs made it difficult to accurately measure their full length. However, we might roughly estimate a minimum length of 100 μm.

HR-TEM images provided us with complementary information to XRD on the crystal nature of CuNWs. Fig. 2D–H show the HR-TEM images of the thinner and the thicker CuNWs of the series (CuNWs@0 and CuNWs@9). No changes in the crystal growth direction, which remained along the ⟨110⟩ direction, were observed when the aspect ratio of CuNWs decreased by increasing the amount of glycine in the synthesis protocol (see Fig. 2D and H).

The selected area electron diffraction (SAED) pattern displayed bright spots representing the (220), (200), and (111) planes in reciprocal space (Table S3). The fringes have lattice spacings reported in Fig. 2E and I. HR-TEM images also reveal the presence of a more transparent surface coating that may be reasonably assigned to an amorphous Cu_2O/CuO oxide layer (approximately 3 nm thick) passivating the CuNWs (Fig. 2D and H), in agreement with prior works.[11,33–37] The assignment of this thin amorphous layer to Cu oxide is strongly supported by both our HR-TEM analysis and extensive prior literature.[11,33–37] Several studies have shown that Cu nanowires and other nanostructured copper materials rapidly develop a native oxide layer typically 1–5 nm thick when exposed to ambient conditions.

To gain further insight into the NW surface morphology, AFM measurements were performed for CuNWs@9 and CuNWs@0. The roughness estimated by AFM of CuNWs@0 and CuNWs@9 was 7 nm and 17 nm respectively (area analyzed 50 nm × 50 nm of the nanocrystal surface) (Fig. 3A, B and Fig. S5, S6), indicating a strong relationship between the surface properties and the CuNW diameter. In addition, the longitudinal profile of the surface (Fig. 4B amd D), measured along the length of CuNWs, reveals the presence of terraces ranging from 2 to 5 nm in height, while measurements taken in the perpendicular direction with respect to the wire main axis show a smooth surface pattern (Fig. 3(1) and (2)), thus highlighting that the steps arise along the NWs' growth direction. Overall, our findings corroborate the role of glycine as an additive reagent enabling tuning of the growth of CuNW diameters up to 400 nm, while maintaining a well-determined crystal structure and nano-roughness.

To investigate how glycine affects the crystal facet structure of the CuNW surfaces, an electrochemical approach based on the different affinity of the OH^- group for the distinctive Cu crystal facet orientations was employed.[22,38–41] Notably, CVs in alkali media have been recently investigated and reconsidered to be a valuable tool to study ideal model surfaces such as low index Cu(100), Cu(110), Cu(111), single crystals,[40–42] and even nanostructures based on Cu and Ag.[43]

Voltammetric patterns of CuNW-based electrodes immersed in a NaOH electrolyte were investigated by considering two electron processes at the surface: specifically, electrosorption of OH^- (eqn (2)) and electro-oxidation of OH^- to O-adsorbed species on Cu (exemplified in (eqn (3)).

$$nCu + OH^- \rightarrow Cu_n(OH)_{ads} + e^- \quad (2)$$

$$Cu_n(OH)_{ads} + OH^- \rightarrow Cu_n(O)_{ads} + H_2O + e^- \quad (3)$$

Fig. 4A shows the voltammetric patterns of CuNWs in the anodic region. The electro-oxidation of OH^- onto the surface facets is observed between +0.30 and +0.50 V *vs.* RHE, and its

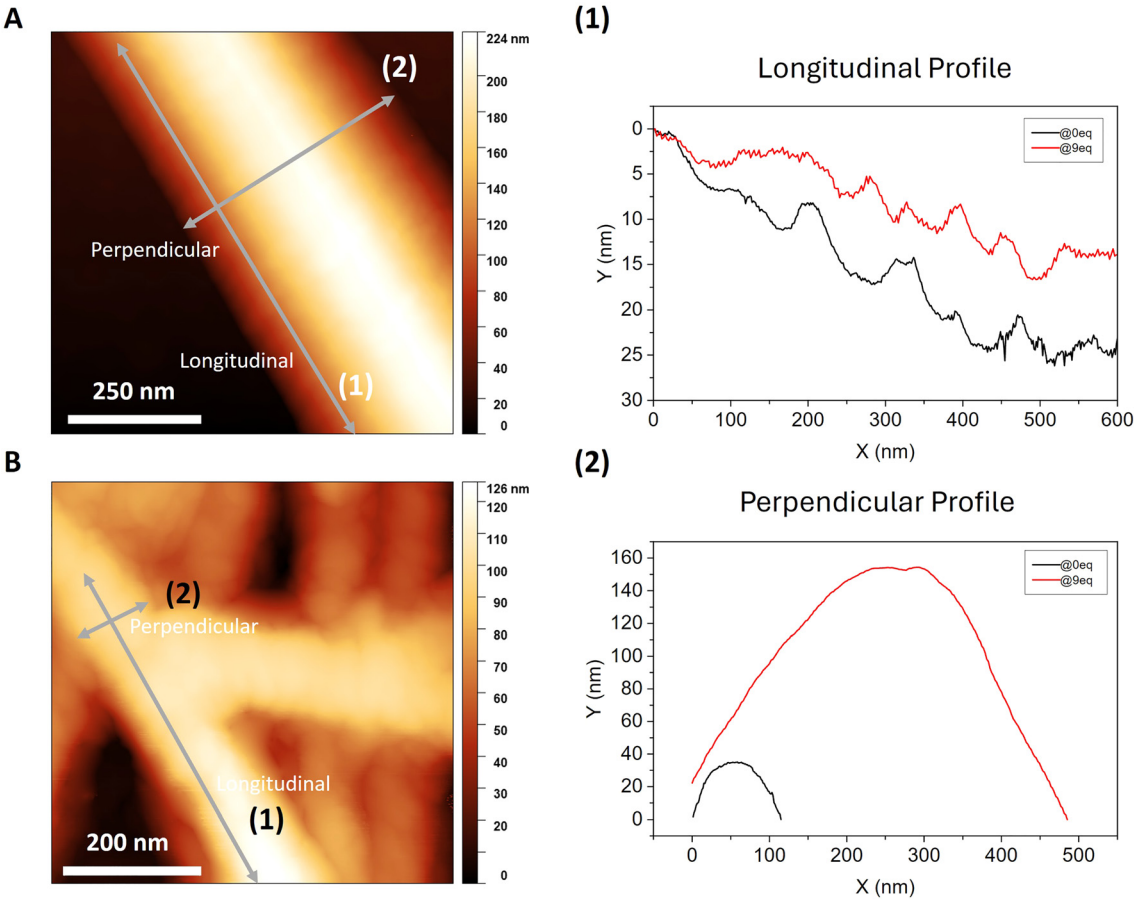

Fig. 3 (A) AFM map of CuNWs@9. (B) AFM map of CuNWs@0. (1) Longitudinal profile recorded for CuNWs@9 and CuNWs@0 types. (2) Perpendicular profile with respect to the growth direction recorded for CuNWs@9 and CuNWs@0 types.

results are strongly affected by the selected inversion potential. By enlarging the potential window further positively than +0.5 V, the oxidation of Cu and the consequent reduction of Cu oxide (Cu_2O formed at the CuNW electrode) in the backward reductive sweep interfere with the detection of the (100), (110), and (111) planes' signals. Therefore, inverting the potential before the oxidation of Cu guarantees obtaining clear and defined peaks in the reduction segment. Furthermore, the adsorption peak area can be reasonably correlated with the relative proportion of exposed facets. Specifically, the percentage of facets on the CuNWs' surface was evaluated by carrying out a deconvolution analysis of the baseline-corrected voltammetric peaks in the potential range from +0.35 to +0.44 V *vs.* RHE (Fig. 4). For each CuNW, a broad peak located at about −0.1 V, which refers to (100)-specific OH^- adsorption, was observed, confirming the presence of this facet (terraces) in our CuNWs.[7,44] This process is represented by eqn (2). Furthermore, the presence of these (100) crystal facets was also confirmed by analyzing the reversible sharp peak at potential values ranging from +0.372 V to +0.376 V *vs.* RHE, which may be ascribed to O-adsorbed species that are generated from OH^- adsorbed as shown in eqn (3). A further broader peak at +0.41 V *vs.* RHE was assigned to the (110) facets, which in the case of our CuNWs may be assigned to steps that create defectiveness on the (100)-type terrace.[40,45,46] A semi-quantitative analysis of voltammograms reveals that the (110) peak increases linearly with the glycine concentration, so that it becomes more pronounced with the increase of the CuNW diameter, suggesting a higher number of steps on the CuNW surface, in agreement with AFM analysis. Importantly, these electrochemical insights give complementary information to that obtained from XRD analysis, which provides information on the crystal structure of the bulk materials, while electrochemistry interrogates only the surface of CuNWs. For CuNWs@0, the electrochemical analysis shows the relative abundance of 63.4% of the (110)-type facet, whereas CuNWs@9 exhibits a relative amount of 85% prevalence. Fig. 5 shows that beyond a certain NW diameter value, the relative amount of the (110) facet reaches a plateau and does not increase further.

The fingerprint of the (111) facets was not clearly detected in any CuNW electrodes. A visual representation of CuNWs' surface crystal facets is shown in Fig. 4H, representing the (100) extended surface typical of CuNWs and the (110) steps along the CuNWs' growth direction. In this pictorial representation of CuNWs' surface, other types of crystal arrangements have also been inserted for exhaustiveness, such as vacancies and islands, which are not excluded from being formed. Overall, the 3D plot in Fig. S7 exemplifies the correlation between

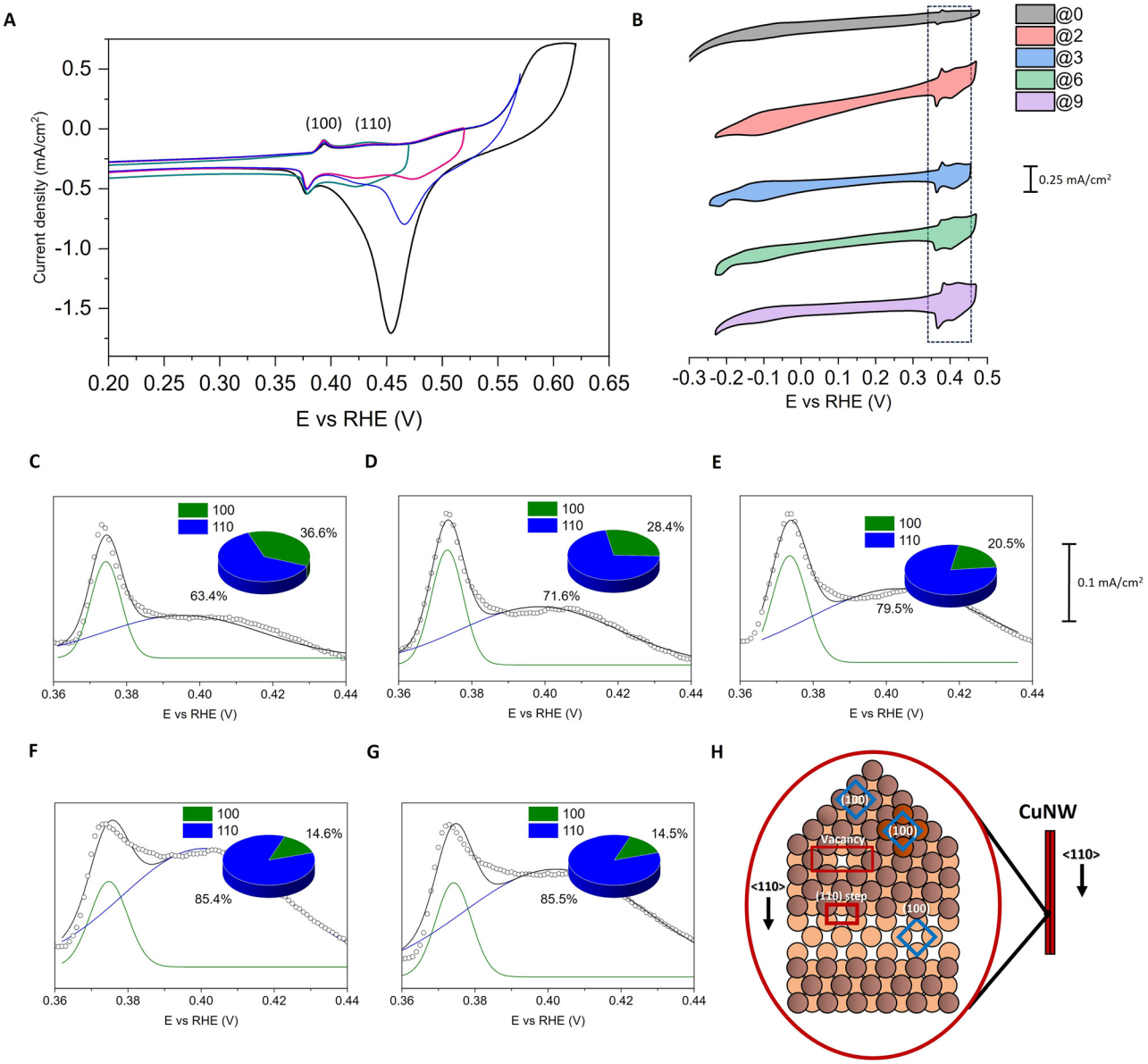

Fig. 4 (A) Cyclic voltammetry results of CuNWs@3 recorded in 1 M NaOH, in a three-electrode cell configuration under an Ar-saturated solution, inverting the oxidation potential at different stages: +0.47 V (green), +0.52 V (magenta), +0.57 V (blue), and +0.62 V (black). (B) Cyclic voltammetries were recorded in 1 M NaOH, in a three-electrode cell configuration under an Ar-saturated solution and atmosphere. The black rectangle represents the magnification region. (C)—(G) Zoom of CV for CuNWs@0 (C), CuNWs@2 (D), CuNWs@3 (E), CuNWs@6 (F), and CuNWs@9 (G) in 1 M NaOH. The dotted curves represent the experiment CV's signals, and the black curves represent the simulated ones. The red and blue curves represent the deconvoluted peaks of the (100) and (110), respectively. (H) Representation of the crystal step (110) on the (100) surface of a CuNW. The dark Cu elements are the first atomic layer of the surface, the lighter represents the second atomic layer, and the dark orange represents the possible defectiveness.

surface exposed facets, CuNWs' diameter, and Ψ, highlighting the intimate interconnection between the morphology of CuNWs, synthesis conditions, and surface crystallographic orientations. In particular, since the growth of CuNWs occurs throughout a dynamic deposition/dissolution equilibrium between Cu ions and Cu^0 on the surface of the Cu(110) facet,[47] our findings confirm that the deposition of Cu ions might occur differently when glycine is employed due to its different coordination modes.[48–54]

Moreover, the observed increase of the (110) steps over the (100) with the increase of the CuNWs' thickness may be also explained with the relative stability of the glycine on (110) with respect to (100), as it has been experimentally and theoretically observed in the past by several groups (see Table S4).[47,48,50,53–55] This, together with the larger roughness detected by AFM, points to an overall picture characterized by a larger defectiveness of the CuNW (100) lateral surfaces that the electrochemical investigation identified as mostly (110)-type steps. In particular, the (110) facets, being more open and less densely packed with respect to (100), have higher surface energy[56] and are less likely to dominate the external surfaces. Furthermore, steps and edges involving unsaturated coordination sites

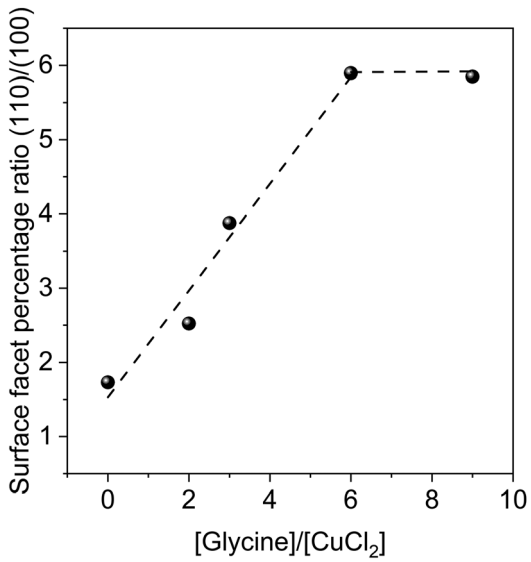

Fig. 5 Dependence of the surface facet ratio on the quantity of glycine used in the synthesis protocol.

translate to the material having higher absorption energy and, most of the time, higher reactivity.

Conclusions

In summary, we synthesized and characterized a family of CuNWs that exhibited a native, pronounced stepped surface that we ascribed to glycine. Our study highlighted indeed that the competitive capping strength between ODA and glycine is the main driving force for the differences in the NWs' morphology. The amine and carboxylic acid groups of glycine adsorb on the nascent Cu surfaces during the growth, thus competitively reducing the amount of ODA bonded onto the CuNW surface. On the other hand, glycine's shorter carbon chain compared to ODA limits its effectiveness as a capping agent, leading to the formation of thicker CuNWs. Additionally, glycine's carboxylic group forms a salt with ODA's amine group, further inhibiting ODA adsorption as the glycine concentration increases. All these phenomena lead to the formation of thicker, but shorter CuNWs as the glycine concentration increases, as we demonstrated using complementary approaches such as XRD, HR-TEM, and cyclic voltammetry. The action of glycine was not limited to modulating the aspect ratio of the CuNWs, but also modified the CuNWs' surface during the synthesis. Overall, our analysis demonstrates a correlation between the amount of glycine employed in the synthesis and the relative quantity of the (100) and (110) facets, together with the aspect ratio, thus shedding light on the subtleties of nanomaterial synthesis. Moreover, a nanoscale surface roughness on the (100)-faceted Cu nanowires was also revealed, highlighting that the CuNW surface is not atomically flat but consists of a pattern of (110)-type steps. Our findings bring potential implications for technological applications such as catalysis, where the presence of surface vacancies, dislocations, and grain boundaries can significantly increase the active surface area, thus lowering the activation energy required for various electrochemical processes. Finally, this controlled synthetic approach overcomes the limitations of traditional bulk copper materials, which commonly suffer from inconsistent surface preparation, labor-intensive polishing processes, and poor reproducibility across different laboratories.

Experimental section

Reagents

All manipulations were carried out in the air using standard laboratory equipment. All the reagents and the solvents were obtained from commercial suppliers and used as received without further purification. Copper dichloride dihydrated ($CuCl_2 \cdot 2H_2O$, >99.0% from Merck), 1-octadecylamine (ODA, 90%, from Merck), glucose (>99.5%, from Merck), glycine (>99%, from Merck), NaOH (>99.0%, from Merck), isopropanol (>99.8%, from Merck), and water (MilliQ, 18.2 MΩ) were used.

CuNWs synthesis

The CuNWs syntheses were performed in a 500 mL flask, closed with a screw cap. A thermostatic oil bath was employed to heat the reaction mixture. Typically, 0.400 g of $CuCl_2 \cdot 2H_2O$ and 2.529 g of 1-octadecylamine (ODA) were added to 200 mL of water. The mixture was mixed and sonicated for 40 minutes at 40 °C. Afterward, two equivalents of glucose with respect to $CuCl_2 \cdot 2H_2O$ were added to the reaction flask and, if needed x equivalents of glycine, mixed, and heated for 18 h at 125 °C, without stirring the solution. The reaction flask was cooled at room temperature. A red-brownish slurry was formed. Dark red CuNWs precipitated and accumulated at the bottom of the reaction flask. The product was centrifuged at 4000 rpm for 5 minutes using 100 mL of deionized water. This procedure was repeated ten times. Further ten centrifugations were carried out using 50 mL of absolute ethanol solvent for each wash. The obtained CuNWs were stored at 20 °C in absolute isopropanol under an argon-saturated atmosphere. All synthesis experiments were performed at least twice, and measurements (*e.g.*, SEM and electrochemical analyses) were conducted on at least two independently prepared samples for each condition.

X-ray diffraction

Film XRD measurements were conducted using a Bruker D8 Advance diffractometer, fitted with a LYNXEYE detector in 1D mode (Department of Chemical Sciences, University of Padova). Diffraction data were acquired by exposing powder samples to Cu-Kα1,2 X-ray radiation. X-rays were generated from a Cu anode supplied with 40 kV and a current of 40 mA. The data were collected over the 30–100° 2θ range with a step size of 0.025° 2θ and a nominal time per step of 0.20 s. Fixed divergence slits of 0.50° were used together with Soller slits with an aperture of 2.34°.

Scanning electron microscopy (SEM)

SEM was performed with a Zeiss Sigma HD microscope, equipped with a Schottky FEG source, one detector for

backscattered electrons and two detectors for secondary electrons (InLens and Everhart Thornley). The microscope is coupled to an EDX detector (from Oxford Instruments, *x*-act PentaFET Precision) for X-ray microanalysis, working in energy dispersive mode. A low accelerating voltage (5 kV) was used to accurately delineate fine surface features and to avoid conductive coatings that can deleteriously modify the surface morphology.

High resolution transmission electron microscopy (HR-TEM)

Measurements were carried out employing a JEOL JEM-F200 S/TEM working at 200 kV equipped with a Cold Field Emission Gun.

Atomic force microscopy (AFM)

Topographic analysis was performed using an Agilent 5500 SPM atomic force microscope in intermittent contact mode equipped with a Mikromasch HQ: XSC11/AL BS probe characterized by a tip of radius of curvature <10 nm, mean force constant 7 N m^{-1} and frequency 133 kHz. The images were acquired at ambient temperature and data were processed using Gwyddion software.

Electrochemical characterization

Cyclic voltammetries were recorded employing a three-electrode cell configuration. The reference electrode (RE) was Hg/HgO (1 M NaOH). The counter electrode (CE) was a platinum wire. The working electrode was a glassy carbon plate (10 mm $\times$ 15 mm) on which CuNWs were dropcast. Cyclic voltammetries were carried out in 1 M NaOH solution. Every experiment was conducted in an argon-saturated solution.

Author contributions

Andrea Conte: methodology, investigation, visualization, conceptualization, data curation, and writing – original draft, review & editing. Sabrina Antonello: supervision, visualization, conceptualization, and writing – review & editing. Marco Baron: supervision, visualization, conceptualization, and writing – review & editing. Sara Bonacchi: supervision, visualization, conceptualization, writing – review & editing, and funding acquisition. Alessandro Aliprandi: supervision, visualization, conceptualization, writing – review & editing, and funding acquisition.

Conflicts of interest

There are no conflicts to declare.

Data availability

The data supporting the findings of this study are available within the article's main text and the SI in the form of tables, figures, images and equations. The supplementary information contains synthesis images, statistical calculations, SEM images, AFM images, and table on recent literatures regarding CuNWs features. See DOI: **https://doi.org/10.1039/d5tc01835h**.

Acknowledgements

S. B. is grateful for the financial support from the University of Padova – Supporting Talent in Research – STARS 2019 ''TimeForResponse'' grant no. 166081. S. B. kindly acknowledges the financial support from the Italian Ministry of University and Research (MUR) under the National Recovery and Resilience Plan (NRRP), funded by the European Union – NextGenerationEU – Grant Assignment Decree no. 2022RSXC9X. S. B. and A. C. are grateful to Basell Poliolefine Italia S.r.l. for financial support. A. A. kindly acknowledges the Research Council (ERC) under the European Union's Horizon 2020 research and innovation program (grant agreement no. 949087).

Notes and references

1 Q. Huang, C. M. Lilley, M. Bode and R. S. Divan, in 2008 8th IEEE Conference on Nanotechnology, IEEE, Arlington, Texas, USA, 2008, pp. 549–552.
2 M. J. Catenacci, C. Reyes, M. A. Cruz and B. J. Wiley, *ACS Nano*, 2018, **12**, 3689–3698.
3 P. Tran, N.-H. Tran and J.-H. Lee, *Sci. Rep.*, 2022, **12**, 8967.
4 A. Conte, M. Baron, S. Bonacchi, S. Antonello and A. Aliprandi, *Nanoscale*, 2023, **15**, 3693–3703.
5 C. Choi, S. Kwon, T. Cheng, M. Xu, P. Tieu, C. Lee, J. Cai, H. M. Lee, X. Pan, X. Duan, W. A. Goddard and Y. Huang, *Nat Catal*, 2020, **3**, 804–812.
6 Z. Wei, S. Yue, S. Gao, M. Cao and R. Cao, *Nano Res.*, 2023, **16**, 7777–7783.
7 A. Conte, A. Rosati, M. Fantin, A. Aliprandi, M. Baron, S. Bonacchi and S. Antonello, *Mater. Adv.*, 2024, **5**, 8836–8846.
8 P. Rohith, G. Sainath and B. K. Choudhary, *Comput. Condensed Matter*, 2018, **17**, e00330.
9 M. J. Kim, Y. Seo, M. A. Cruz and B. J. Wiley, *ACS Nano*, 2019, **13**, 6998–7009.
10 A. Aliprandi, T. Moreira, C. Anichini, M. Stoeckel, M. Eredia, U. Sassi, M. Bruna, C. Pinheiro, C. A. T. Laia, S. Bonacchi and P. Samorì, *Adv. Mater.*, 2017, **29**, 1703225.
11 S. Ye, I. E. Stewart, Z. Chen, B. Li, A. R. Rathmell and B. J. Wiley, *Acc. Chem. Res.*, 2016, **49**, 442–451.
12 F. Yang, M. J. Kim, M. Brown and B. J. Wiley, *Adv. Energy Mater.*, 2020, **10**, 2001174.
13 K. Yu, X. Pan, G. Zhang, X. Liao, X. Zhou, M. Yan, L. Xu and L. Mai, *Adv. Energy Mater.*, 2018, **8**, 1802369.
14 S. Bhanushali, P. Ghosh, A. Ganesh and W. Cheng, *Small*, 2015, **11**, 1232–1252.
15 R. Man, M. Xia, H. Li, F. Tian, J. Zhang, Z. Yu and B. Tang, *Adv. Healthcare Mater.*, 2024, 2401078.
16 S. Wu, Q. Wang, Y. Li, B. Liu and Y. Miao, *Adv. NanoBiomed. Res.*, 2024, **4**, 2400018.
17 E. Plaza-Mayoral, V. Okatenko, K. N. Dalby, H. Falsig, I. Chorkendorff, P. Sebastián-Pascual and M. Escudero-Escribano, *iScience*, 2024, **27**, 109933.
18 I. E. L. Stephens, K. Chan, A. Bagger, S. W. Boettcher, J. Bonin, E. Boutin, A. K. Buckley, R. Buonsanti,

E. R. Cave, X. Chang, S. W. Chee, A. H. M. Da Silva, P. De Luna, O. Einsle, B. Endrődi, M. Escudero-Escribano, J. V. Ferreira De Araujo, M. C. Figueiredo, C. Hahn, K. U. Hansen, S. Haussener, S. Hunegnaw, Z. Huo, Y. J. Hwang, C. Janáky, B. S. Jayathilake, F. Jiao, Z. P. Jovanov, P. Karimi, M. T. M. Koper, K. P. Kuhl, W. H. Lee, Z. Liang, X. Liu, S. Ma, M. Ma, H.-S. Oh, M. Robert, B. R. Cuenya, J. Rossmeisl, C. Roy, M. P. Ryan, E. H. Sargent, P. Sebastián-Pascual, B. Seger, L. Steier, P. Strasser, A. S. Varela, R. E. Vos, X. Wang, B. Xu, H. Yadegari and Y. Zhou, *J. Phys. Energy*, 2022, **4**, 042003.

19 A. Auer, M. Andersen, E.-M. Wernig, N. G. Hörmann, N. Buller, K. Reuter and J. Kunze-Liebhäuser, *Nat. Catal.*, 2020, **3**, 797–803.

20 Z. Zhou, X. Li, Q. Li, Y. Zhao and H. Pang, *Mater. Today Chem.*, 2019, **11**, 169–196.

21 X. Zhang, Y. Wang, C. Liu, Y. Yu, S. Lu and B. Zhang, *Chem. Eng. J.*, 2021, **403**, 126269.

22 Y.-C. Zhang, X.-L. Zhang, Z.-Z. Wu, Z.-Z. Niu, L.-P. Chi, F.-Y. Gao, P.-P. Yang, Y.-H. Wang, P.-C. Yu, J.-W. Duanmu, S.-P. Sun and M.-R. Gao, *Proc. Natl. Acad. Sci. U.S.A.*, 2024, **121**, e2400546121.

23 D. Zheng, Y.-Q. He, H. Ou-Yang, J.-D. Zhang, G. Zhang and S.-K. Han, *Nano Lett.*, 2024, **24**, 8887–8893.

24 T. Zhang, W.-Y. Hsieh, F. Daneshvar, C. Liu, S.-P. Rwei and H.-J. Sue, *Nanoscale*, 2020, **12**, 17437–17449.

25 M. Kevin, G. Y. R. Lim and G. W. Ho, *Green Chem.*, 2015, **17**, 1120–1126.

26 Y.-K. Kim, Y.-J. Yu, S.-H. Kim and J.-Y. Choi, *J. Mater. Sci.*, 2024, **59**, 11718–11731.

27 B. Bhagat, V. Jadeja, P. Sharma, R. Bandyopadhyay and K. Mukherjee, *Mater. Sci. Eng.: B*, 2022, **286**, 116027.

28 G. M. O'Connor, K. Lepkova, J. J. Eksteen and E. A. Oraby, *Hydrometallurgy*, 2018, **181**, 221–229.

29 Y. Y. He, M. Luo, X. Y. Zhang and J. Meng, *Electrochim. Acta*, 2015, **165**, 416–421.

30 S. Aksu and F. M. Doyle, *J. Electrochem. Soc.*, 2001, **148**, B51–B57.

31 F. Habashi, *J. Chem. Educ.*, 1965, **42**, 318.

32 D. V. Ravi Kumar, I. Kim, Z. Zhong, K. Kim, D. Lee and J. Moon, *Phys. Chem. Chem. Phys.*, 2014, **16**, 22107–22115.

33 D. Mardiansyah, T. Badloe, K. Triyana, M. Q. Mehmood, N. Raeis-Hosseini, Y. Lee, H. Sabarman, K. Kim and J. Rho, *Sci. Rep.*, 2018, **8**, 10639.

34 F. Teng, L. Zheng, K. Hu, H. Chen, Y. Li, Z. Zhang and X. Fang, *J. Mater. Chem. C*, 2016, 8416–8421.

35 O. Ohiienko and Y.-J. Oh, *Mater. Chem. Phys.*, 2020, **246**, 122783.

36 L. Xu, Y. Yang, Z.-W. Hu and S.-H. Yu, *ACS Nano*, 2016, **10**, 3823–3834.

37 C. Celle, A. Cabos, T. Fontecave, B. Laguitton, A. Benayad, L. Guettaz, N. Pélissier, V. H. Nguyen, D. Bellet, D. Muñoz-Rojas and J.-P. Simonato, *Nanotechnology*, 2018, **29**, 085701.

38 K. J. P. Schouten, E. P. Gallent and M. T. M. Koper, *J. Electroanal. Chem.*, 2013, **699**, 6–9.

39 G. Zhang, Z.-J. Zhao, D. Cheng, H. Li, J. Yu, Q. Wang, H. Gao, J. Guo, H. Wang, G. A. Ozin, T. Wang and J. Gong, *Nat. Commun.*, 2021, **12**, 5745.

40 A. K. Engstfeld, T. Maagaard, S. Horch, I. Chorkendorff and I. E. L. Stephens, *Chem. – Eur. J.*, 2018, **24**, 17743–17755.

41 A. Tiwari, H. H. Heenen, A. S. Bjørnlund, T. Maagaard, E. Cho, I. Chorkendorff, H. H. Kristoffersen, K. Chan and S. Horch, *J. Phys. Chem. Lett.*, 2020, **11**, 1450–1455.

42 A. Bagger, R. M. Arán-Ais, J. Halldin Stenlid, E. Campos Dos Santos, L. Arnarson, K. Degn Jensen, M. Escudero-Escribano, B. Roldan Cuenya and J. Rossmeisl, *Chem. Phys. Chem.*, 2019, **20**, 3096–3105.

43 A. Conte, S. Bonacchi and S. Antonello, *ACS Electrochem*, 2025, DOI: **10.1021/acselectrochem.5c00172**.

44 S. Liu, Y. Li, D. Wang, S. Xi, H. Xu, Y. Wang, X. Li, W. Zang, W. Liu, M. Su, K. Yan, A. C. Nielander, A. B. Wong, J. Lu, T. F. Jaramillo, L. Wang, P. Canepa and Q. He, *Nat. Commun.*, 2024, **15**, 5080.

45 S. J. Raaijman, N. Arulmozhi, A. H. M. Da Silva and M. T. M. Koper, *J. Electrochem. Soc.*, 2021, **168**, 096510.

46 D. Hochfilzer, A. Tiwari, E. L. Clark, A. S. Bjørnlund, T. Maagaard, S. Horch, B. Seger, I. Chorkendorff and J. Kibsgaard, *Langmuir*, 2022, **38**, 1514–1521.

47 S. M. Barlow, K. J. Kitching, S. Haq and N. V. Richardson, *Surf. Sci.*, 1998, **401**, 322–335.

48 J. W. Han, J. N. James and D. S. Sholl, *J. Chem. Phys.*, 2011, **135**, 034703.

49 V. Feyer, O. Plekan, N. Tsud, V. Lyamayev, V. Cháb, V. Matolín, K. C. Prince and V. Carravetta, *J. Phys. Chem. C*, 2010, **114**, 10922–10931.

50 J. Hasselstrom, O. Karis, M. Weinelt, N. Wassdahl, A. Nilsson, M. Nyberg, L. G. M. Petterson, M. G. Samant and J. Stohr, *Surf. Sci.*, 1998, **407**, 221–236.

51 X. Zhao, Z. Gai, R. G. Zhao, W. S. Yang and T. Sakurai, *Surf. Sci.*, 1999, **424**, L347–L351.

52 V. Efstathiou and D. P. Woodruff, *Surf. Sci.*, 2003, **531**, 304–318.

53 V. Carravetta, S. Monti, C. Li and H. Ågren, *Langmuir*, 2013, **29**, 10194–10204.

54 M. Sacchi, D. J. Wales and S. J. Jenkins, *Phys. Chem. Chem. Phys.*, 2017, **19**, 16600–16605.

55 A. D. Ievins, M. Sacchi and S. J. Jenkins, *ACS Omega*, 2025, **10**, 7422–7427.

56 Z. Wang, G. Yang, Z. Zhang, M. Jin and Y. Yin, *ACS Nano*, 2016, **10**, 4559–4564.

